TISSUE ENGINEERING: Part A
Volume 22, Numbers 7 and 8, 2016

DOI: 10.1089/ten.tea.2015.0417

termis
Tissue Engineering
& Regenerative Medicine
International Society

ORIGINAL ARTICLE

Enhanced Bone Repair by Guided Osteoblast Recruitment Using Topographically Defined Implant

Jeong-Kee Yoon, BS,[1,*] Hong Nam Kim, PhD,[2,3,*] Suk Ho Bhang, PhD,[4] Jung-Youn Shin, PhD,[1] Jin Han, MS,[1] Wan-Geun La, PhD,[5] Gun-Jae Jeong, BS,[1] Seokyung Kang, MS,[1] Ju-Ro Lee, BS,[1] Jaesur Oh, BS,[1] Min Sung Kim, PhD,[3] Noo Li Jeon, PhD,[3] and Byung-Soo Kim, PhD[1,6]

The rapid recruitment of osteoblasts in bone defects is an essential prerequisite for efficient bone repair. Conventionally, osteoblast recruitment to bone defects and subsequent bone repair has been achieved using growth factors. Here, we present a methodology that can guide the recruitment of osteoblasts to bone defects with topographically defined implants (TIs) for efficient *in vivo* bone repair. We compared circular TIs that had microgrooves in parallel or radial arrangements with nonpatterned implants for osteoblast migration and *in vivo* bone formation. *In vitro,* the microgrooves in the TIs enhanced both the migration and proliferation of osteoblasts. Especially, the microgrooves with radial arrangement demonstrated a much higher efficiency of osteoblast recruitment to the implants than did the other types of implants, which may be due to the efficient guidance of cell migration toward the cell-free area of the implants. The expression of the intracellular signaling molecules responsible for the cell migration was also upregulated in osteoblasts on the microgrooved TIs. *In vivo*, the TI with radially defined topography demonstrated much greater bone repair in mouse calvarial defect models than in the other types of implants. Taken together, these results indicate that implants with physical guidance can enhance tissue repair by rapid cell recruitment.

Introduction

Tissue defects are repaired in a series of steps, which include the infiltration of host reparative cells (e.g., osteoblast and fibroblast) into the defect site, the proliferation and activation of the cells, and the deposition of extracellular matrices (ECMs) in the defects.[1–3] Among these steps, the rapid recruitment of host reparative cells is required for efficient tissue repair because the rapid initiation reduces the time required for subsequent steps. In the body, the host reparative cells near the damaged tissues are recruited into the damaged region by the cell tropic factor gradient, which is generated by the secretion of various growth factors and cytokines by the body when the tissues are damaged.[4]

Inspired by such a chemotaxis mechanism, the delivery of biochemical factors in the damaged site has become a widely used methodology that facilitates tissue repair by enhancing host cell recruitment, proliferation, and activation. Specifically for bone repair, platelet-derived growth factor (PDGF),[5–7] transforming growth factor-β (TGF-β),[5,6] and bone morphogenetic protein-2 (BMP-2)[8] have been used to manipulate cell behaviors. The chemotactic cue-induced bone repair methods can prevent the migration of other types of cells, such as epithelial cells.[9] However, the utilization of chemical cues still poses several limitations, such as the high cost of growth factors, the short half-life of growth factor proteins *in vivo*, and the potential adverse effects of overdose events or pathological conditions.[10]

As an alternative method, physical guidance can be used to promote tissue repair. It has been shown that the micro- or nanoscale topography can affect not only the apparent behaviors of the cells, such as the direction or speed of migration, but also the functions of the cells, such as their signaling and differentiation.[11] Based on the *in vitro* results presented in previous studies, several studies have attempted the *in vivo* application of scaffolds with topography.[12] However, the studies focused primarily on engineering the

[1]School of Chemical and Biological Engineering, Seoul National University, Seoul, Republic of Korea.
[2]Center for BioMicrosystems, Brain Science Institute, Korea Institute of Science and Technology (KIST), Seoul, Republic of Korea.
[3]School of Mechanical and Aerospace Engineering, Seoul National University, Seoul, Republic of Korea.
[4]School of Chemical Engineering, Sungkyunkwan University, Suwon, Republic of Korea.
[5]Department of Nanobiomedical Science, Dankook University, Chungnam, Republic of Korea.
[6]Bio-MAX Institute, Institute of Chemical Processes, Seoul National University, Seoul, Republic of Korea.
*These authors contributed equally to this work.

feature size or the surface coating. Thus, their approaches do not consider efficient cell migration.

In this study, we propose a topographically defined implant (TI) that can guide the migratory direction of the cells for the efficient recruitment of osteoblasts into the bone defect. For this purpose, we designed TIs with microgrooves of different arrangement, such as parallel (denoted as line) and radial (denoted as radial). Nonpatterned implants (denoted as flat) were also prepared as a control. First, the migration and proliferation of osteoblasts on the three different TIs were compared *in vitro*. The intracellular molecular signaling was also examined to investigate the signaling mechanisms of the cell migration results. Second, we determined whether the implants with physical guidance can enhance bone tissue repair by implanting the TIs in mouse calvarial defect models.

Materials and Methods

Fabrication of TIs

TIs with microgrooves with line and radial topographies (pits that were 5 μm in both width and depth), as well as a flat type, were fabricated by using a capillary molding technique (Fig. 1).[13] To fabricate a flexible mold, 10 μL of polyurethane acrylate (PUA; Minuta Technology, Seoul, South Korea) was dispensed on the prepatterned silicon master, which was prepared by photolithography and deep reactive ion etching. Then, a 50-μm-thick polyethylene terephthalate (PET) film was brought into contact onto the drop. After mild pressing ($\sim$100 Pa) with a roller, ultraviolet (UV) light ($\lambda = 365$ nm, power = 4.3 mW) was irradiated for 50 s,[14,15] and the cured pattern backed with a PET film (a flexible mold) was peeled off from the master. Then, the flexible mold containing the reversed pattern of the silicon master was cured overnight to complete surface cross-linking.

TIs for *in vivo* and *in vitro* studies were prepared by replicating patterns of the flexible mold, thus reconstituting the original pattern on a target substrate. The topography was fabricated on glass coverslips for *in vitro* studies in the same manner ($\lambda = 365$ nm, power = 4.3 mW) except UV irradiation time period (30 s) using Norland Optical Adhesive (NOA) 86 (Norland Products, New Brunswick, NJ) as a polymer precursor. We set the UV irradiation time period

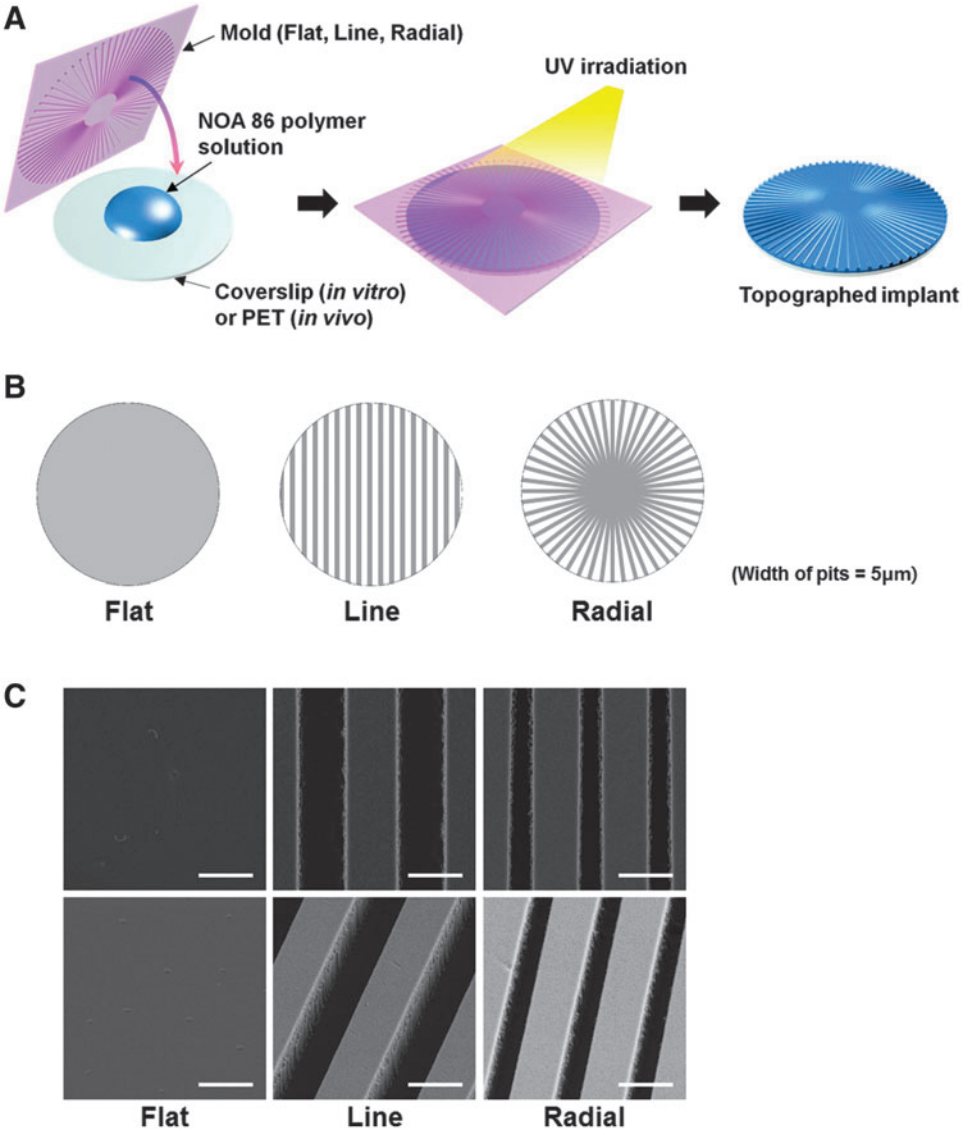

FIG. 1. Schematic diagrams for **(A)** the process of fabrication of the three types of TIs and **(B)** the patterns of the TIs having microgrooves with parallel lines and radial arrangements, as well as a nonpatterned flat implant. The width and depth of the microgrooves were 5 μm. The width at the edge for the radial implant was 5 μm. **(C)** FESEM images of the three types of TIs in both bird's-eye views (*first row*) and tilted views (*second row*) at a magnification of ×10,000. Scale bars indicate 5 μm. FESEM, field emission scanning electron microscopy; TI, topographically defined implant. Color images available online at www.liebertpub.com/tea

for crosslinking of NOA (30 s) shorter than that of PUA (50 s) due to two reasons. First, the total irradiation dose required for crosslinking of NOA (1–10 mJ/cm^2) is lower than that of PUA (100 mJ/cm^2).[14–16] Second, NOA is less affected by oxygen, which inhibits the curing process by scavenging reactive free radicals during photopolymerization, compared to PUA.[17,18] The film-type topography for *in vivo* studies was fabricated on PET films (thickness of 50 μm), using NOA 86 as a polymer precursor. The morphologies of the TIs were examined by field emission scanning electron microscopy (FESEM, SUPRA 55VP; Carl Zeiss, Wetzlar, Germany).

Calcium phosphate coating on TIs

To enhance the osteoconductivity, the TIs were coated with calcium phosphate by immersing them in simulated body fluid (SBF).[19] A volume of 200 mL of 5X SBF solution was prepared using a common method.[20] The surfaces of the TIs were pretreated with oxygen plasma (60 W, PDC-32G; Harrick Scientific, Ossining, NY). Then, the TIs were immersed in 5X SBF for 3 h at room temperature before being coated with calcium phosphate. The surface morphologies and calcium composition of the SBF-treated TIs were compared with those of the untreated TIs. For imaging purposes, the surface of TIs was coated by gold sputtering and observed with field emission scanning electron microscopy and energy dispersive spectroscopy (FESEM/EDS, SUPRA 55VP; Carl Zeiss). To quantify the amount of calcium in the SBF-treated TIs ($n=3$), the TIs were rinsed twice with deionized water and incubated in 0.6 N HCl for 4 h.[21] The calcium was extracted by shaking the sample for 4 h at 4°C. The lysate was subsequently centrifuged at 1000 *g* for 5 min, and the supernatant was used to determine the calcium amount. The calcium concentration in the lysate was quantified spectrophotometrically with cresolphthalein complexone (Sigma, St. Louis, MO). Three minutes after the addition of the reagents, the samples were measured at 575 nm using a microplate reader (PowerWave X340; Bio-Tek Instruments, Inc., Winooski, VT). The calcium concentration was calculated from a standard curve that was generated from the serial dilution of a standard calcium solution (Sigma).

Quantified reverse transcription-polymerase chain reaction

The cytotoxicity of three types of TIs was evaluated by culturing MC3T3-E1 cells on the TIs for 2 days. Quantified reverse transcription-polymerase chain reaction (qRT-PCR) was used to quantify the relative gene expression levels of BCL2-associated X (*Bax*) and B-cell lymphoma 2 (*Bcl-2*). The total RNA was extracted from the samples ($n=4$) using 1 mL of TRIzol reagent (Invitrogen, Carlsbad, CA) and 200 μL of chloroform. The lysed samples were centrifuged at 12,000 rpm for 10 min at 4°C. The RNA pellet was washed with 75% (v/v) ethanol in water and dried. After drying, samples were dissolved in RNase-free water. For qRT-PCR, the iQ™ SYBR Green Supermix kit (Bio-Rad, Hercules, CA) and the MyiQ™ Single-Color Real-Time PCR Detection System (Bio-Rad) were used. β-actin served as the internal control.

In vitro *cell migration study*

A thin polydimethylsiloxane (PDMS) sheet (diameter of 5 mm, thickness of ~100 μm) was attached at the center of the TIs to prevent cell adhesion on the masked region. MC3T3-E1 cells (mouse osteoblast cell line; ATCC, Manassas, VA) were seeded on the TIs and cultured until they reached a confluent monolayer with Dulbecco's modified Eagle's medium high glucose (Gibco BRL, Gaithersburg, MD) supplemented with 10% (v/v) fetal bovine serum (Gibco BRL) and 1% (v/v) penicillin/streptomycin (Gibco BRL). Removal of the PDMS sheets allowed for the migration and proliferation of the cells toward the empty, cell-free area of the TIs, and the time-dependent cell migration area was monitored for 2 days. The area of the cell-free zone was calculated using an image analysis system coupled to a light microscope ($n=3$).

Immunocytochemistry

The cells on the substrates were fixed with 4% paraformaldehyde for 10 min at room temperature and washed with phosphate-buffered saline (PBS). A primary antibody against caspase-3 (Abcam, Cambridge, MA) diluted in 10% bovine serum albumin-containing PBS was incubated for 1 h. Then, the samples were washed three times with PBS and subsequently incubated with rhodamine (TRITC)-conjugated secondary antibodies (Jackson-ImmunoResearch, West Grove, PA) for 1 h at room temperature. All samples were mounted with a mounting solution containing 4,6-diamidino-2-phenylindole (DAPI; Vector Laboratories, Burlingame, CA) to stain the nuclei and photographed using a fluorescent microscope (IX71; Olympus, Tokyo, Japan).

Phalloidin staining

Phalloidin staining was performed to determine F-actin alignment in MC3T3-E1 cells ($n=3$) using an Actin Cytoskeleton and Focal Adhesion Staining Kit (FAK100; Millipore, Billerica, MA) according to the manufacturer's instructions. The images were photographed using a confocal scanning laser microscope (Carl Zeiss-LSM700; Carl Zeiss International, Oberkochen, Germany). The orientations of the cells and F-actin were analyzed by comparing the major axis of the cell body and the angle of the actin filament with the orientation of the underlying microgrooves. The distributions of the angles were analyzed using the ImageJ software (National Institute of Health, Bethesda, MD).

Time lapse microscopy

Time lapse microscopy was performed with an inverted microscope (IX81, Olympus) fitted with an environmentally controlled imaging chamber (Live Cell Instrument, Seoul, Korea). The chamber was maintained at 37°C with 5% CO_2. The migration of MC3T3-E1 cells was observed for 12 h after removing PDMS from the center of the TIs. The images were taken every 15 min, and the migration distance from the initial position of the randomly selected cells was quantified. The migration speed of the randomly selected cells was also quantified by dividing the migration distance by 12 h. All analyses using sequential images were processed with the Gradientech Tracking Tool™ (Gradientech AB, Uppsala, Sweden).

Western blot analysis

The molecular signaling and proliferation during migration of MC3T3-E1 cells were evaluated by determining protein expression of the relevant markers using western blot analysis. The migrating cells on the TIs ($n=4$ samples per group) were washed three times with PBS (Gibco-BRL) and lysed by adding the sodium dodecyl sulfate (SDS) sample buffer [62.5 mM Tris–HCl (pH 6.8), 2% SDS, 10% glycerol, 50 mM dithiothreitol, 0.1% Bromophenol Blue]. The proteins in the buffer were electrophoretically separated on 4–10% SDS polyacrylamide gels and transferred to membranes (Millipore, Bedford, MA). For the protein detection, the membranes were incubated with primary antibodies against epithelial cadherin (E-cadherin), ras-related C3 botulinum toxin substrate 1 (Rac1), phosphatidylinositol-4,5-bisphosphate 3-kinase (PI3K), protein kinase B (Akt), phosphorylated Akt (pAkt), proliferating cell nuclear antigen

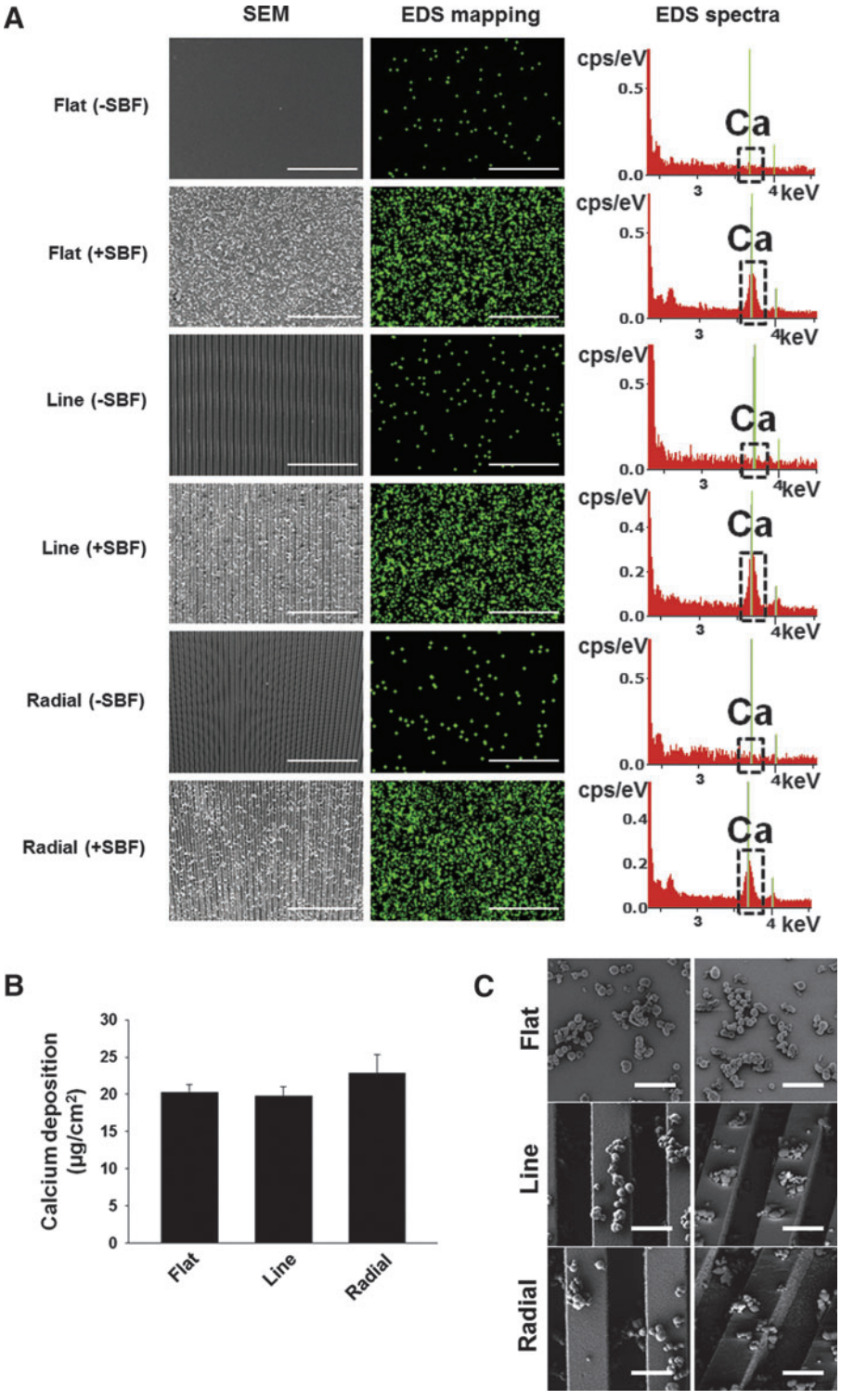

FIG. 2. Coating of three types of TIs with calcium phosphate by immersing the TIs in SBF. **(A)** Confirmation of calcium phosphate coating on the TIs by SEM, EDS mapping, and EDS analyses before and after immersion of the TIs in SBF. TIs were immersed in a 5X SBF solution for 3 h. **(B)** The content of calcium deposited on TIs after immersion in SBF ($n=3$). No significant difference was observed among the three different types of TIs. **(C)** The calcium phosphate particles on the TIs were examined by FESEM in both bird's-eye views (*first column*) and tilted views (*second column*) at a higher magnification (×10,000). The scale bars indicate 5 μm. EDS, energy dispersive spectroscopy; SBF, simulated body fluid. Color images available online at www.liebertpub.com/tea

(PCNA), and β-actin (all antibodies from Abcam) for overnight at 4°C. Then, the membranes were washed and incubated with secondary antibodies conjugated to horseradish peroxidase (Sigma) for 50 min at room temperature. The blots were developed using enhanced chemiluminescence (Lumi-GLO; KPL Europe, Guildford, United Kingdom), as recommended by the manufacturer.

In vivo *calvarial bone repair*

Six-week-old ICR (Institute of Cancer Research) mice (Koatech, Kyunggi-do, Korea) were anesthetized with xylazine (20 mg/kg) and ketamine (100 mg/kg). After shaving the scalp hairs, a longitudinal incision was made in the midline of the cranium from the nasal bone to the posterior nuchal line, and the periosteum was elevated to expose the surface of the parietal bones. Using a surgical trephine bur (Ace Surgical Supply Co., Brockton, MA) and a low-speed micromotor, two circular and transosseous defects with a diameter of 4 mm, the critical size of mouse calvarial defect,[22] were produced in the skull. The drilling sites were irrigated with saline and the bleeding points were electrocauterized. TIs were placed on the calvarial defects ($n=8$ defects per group) and fixed using fibrin gel (Greenplast®; Yongin, Kyunggi-do, South Korea). The skin was then closed with resorbable 6–0 vicryl sutures (Ethicon, Edinburgh, United Kingdom). The animal study was approved by the Institutional Animal Care and Use Committee of Seoul National University (SNU-140509–8).

Bone formation analysis

Seven weeks after the implantation of the TIs, the mice were sacrificed. The skulls were retrieved and fixed in 4% paraformaldehyde. The extent of bone formation was evaluated using microcomputed tomography (micro-CT) scanning ($n=8$ implants per group, SkyScan-1172; Skyscan, Kontich, Belgium) and histological analysis. The micro-CT system was operated at a voltage of 40 kV and a current of 250 mA. For the histological analysis ($n=8$ implants per group), the specimens were embedded in paraffin and sectioned transversely to obtain 4-mm-thick sections. The sections were examined after the Goldner's trichrome staining. The area of bone formation was measured using an image analysis system coupled to a light microscope. The bone formation area was expressed as the percentage of reparated bone area of the total cross-sectional area [(bone area/total area) × 100%].[23]

Statistical analysis

All quantitative data are expressed as the mean ± standard deviation. A one-way analysis of variance (ANOVA) using the Bonferroni test was performed to determine significant differences. The assumptions of ANOVA were found to satisfy Levene's test for homogeneity of variance and to pass tests for normality. A value of $p<0.05$ was considered statistically significant.

Results

The preparation of TIs

NOA 86 was chosen as a material for the TIs because of its elastic modulus, which is similar to that of the natural calvaria.[24] The three types of TIs (Fig. 1B) were examined by FESEM in both bird's-eye views and tilted views, confirming that no creeping phenomena were induced (Fig. 1C). Because the polymeric material lacks osteoconductivity,[25] the TIs were coated with calcium phosphate by immersing them in SBF[20] to enhance osteoconductivity.[26] The topography and chemical composition of the TIs with or without calcium phosphate coating were analyzed by using FESEM/EDS (Fig. 2A). Immersing the TIs in SBF resulted in coating of the TI surface with calcium phosphate particles. For the quantification of the calcium content, EDS mapping was used. The EDS mapping (green signals in the second column of Fig. 2A) showed that the TIs immersed in SBF were coated with calcium. In addition, the EDS spectra showed the calcium peak only on the surface of TIs immersed in SBF (third column of Fig. 2A). The quantification of deposited calcium amount showed that $\sim 20\,\mu g/cm^2$ of calcium was deposited on the surfaces of all TIs and that there was no significant difference in the deposited calcium amount between the different types of implants (Fig. 2B). The calcium phosphate particles on the TIs were observed by FESEM at a higher magnification (X10,000) in both bird's-eye views and tilted views (Fig. 2C). The size of the particles was much smaller than the topographic pits. Thus,

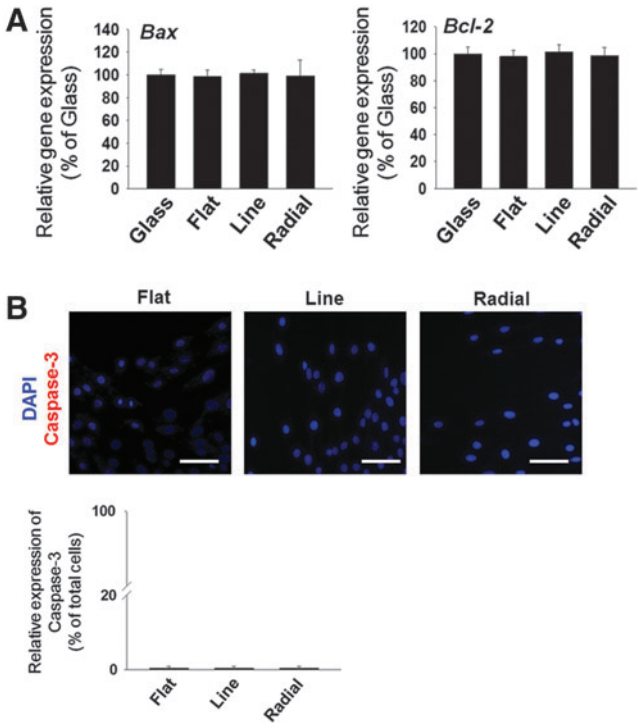

FIG. 3. Cytotoxicity of three types of TIs as evaluated by the culturing of MC3T3-E1 cells on the TIs for 2 days. **(A)** qRT-PCR analyses for expressions of a proapoptotic gene (*Bax*) and an antiapoptotic gene (*Bcl-2*). The expression levels were normalized to those of the glass group ($n=4$). No significant difference was observed among the three different types of TIs. **(B)** Apoptotic activity of MC3T3-E1 cells on the TIs as evaluated by immunocytochemistry for caspase-3 (*red*). *Blue* indicates nucleus (DAPI). Scale bars indicate 100 μm. No significant difference was observed among the three different types of TIs. qRT-PCR, quantified reverse transcription-polymerase chain reaction. Color images available online at www.liebertpub.com/tea

it seems that the pits were not significantly obscured by the calcium phosphate coating. Furthermore, the calcium phosphate particles were evenly distributed on the pits or grooves of the TIs.

Cytotoxicity of NOA 86-based TIs

Before the use of the TIs for the *in vitro* cell migration study and the *in vivo* study, we evaluated the cytotoxicity of the TIs. To date, no study has reported the cytotoxicity or biocompatibility of NOA 86. In this study, the cytotoxicity of NOA 86 was evaluated by examining expressions of various apoptosis markers in MC3T3-E1 cells cultured on NOA 86-based TIs. qRT-PCR analysis showed that the gene expression levels of *Bax* (a proapoptotic marker) and *Bcl-2* (an antiapoptotic marker) on all TIs were not significantly different from those of MC3T3-E1 cells cultured on glass coverslips (a negative control group) (Fig. 3A). Furthermore, the immunocytochemistry for caspase-3 (a proapoptotic marker) showed no difference between the TIs (Fig. 3B). Therefore, NOA 86 has no significant cytotoxicity.

Cell alignment on the patterned substrates

To make a cell-free area on the TIs for cell migration, a PDMS sheet with a diameter of 5 mm was placed as a mask at the center of the TIs (Fig. 4A). After MC3T3-E1 cell plating and removal of the PDMS sheet, the cells were allowed to migrate toward the empty area at the center of the TIs for 2 days. The orientation of the MC3T3-E1 cells at day

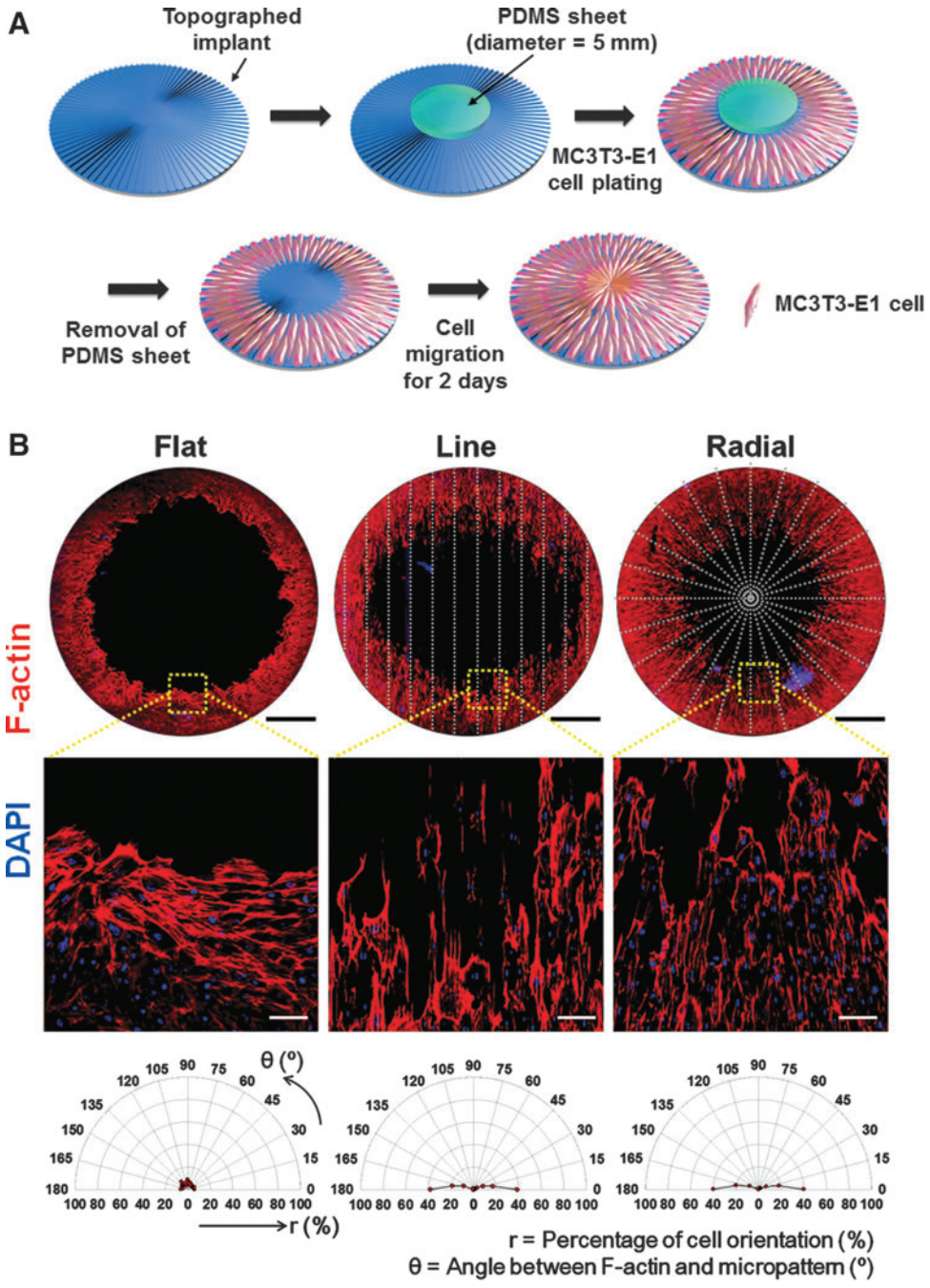

FIG. 4. Alignment of MC3T3-E1 cells on TIs during *in vitro* cellular migration. **(A)** Schematic diagram of the *in vitro* cell migration assay, mimicking *in vivo* host cell migration to calvarial defects. **(B)** F-actin staining (phalloidin staining, *red*) of migrating cells on the TIs at day 2. The *first row* shows the large-area images of TIs with migrating cells. The topographic patterns of the TIs are represented with *gray dotted lines*. Scale bars indicate 1 mm. The *second row* shows the enlarged images of the *yellow square* areas of the TIs with migrating cells. Scale bars indicate 100 μm. *Blue* (DAPI) indicates the nucleus of MC3T3-E1 cells. The *third row* shows the quantification of cell alignment by determining the angles between the F-actin-stained cells and the direction of microgrooves. Color images available online at www.liebertpub.com/tea

2 was evaluated by phalloidin staining (Fig. 4B). The cells on the TIs with line and radial patterns exhibited aligned morphologies along the orientation of the micropatterned topography. In contrast, no alignment of the cells was observed on the flat TIs. The quantification of cell alignment revealed that the cells on the line and radial topographies showed that ~80% of the cells were aligned along the orientation of the microgrooves.

In vitro *cell migration assay*

Time lapse microscopy was used to evaluate the trajectories and speed of MC3T3-E1 cell migration on three different types of TIs (Fig. 5A). The plots clearly showed that cells on the radial TI migrated along the orientation of the microgrooves, whereas the cells on the flat TI demonstrated random migration. On the TI with line patterns, cell migration trajectories showed position-dependent behaviors. In detail, the cells on the top and bottom side of the line topography showed a migration profile similar to that of the cells on the radial pattern, migrating along the orientation of the microgrooves, whereas the cells on the left and right sides of the TI with lines showed a very slow migration. The cells on the line and radial patterns showed a significant increase in migration distances and migration speeds compared with the flat TI (Fig. 5A). However, there was no significant difference in migration distance and speed between the TIs with line and radial topographies.

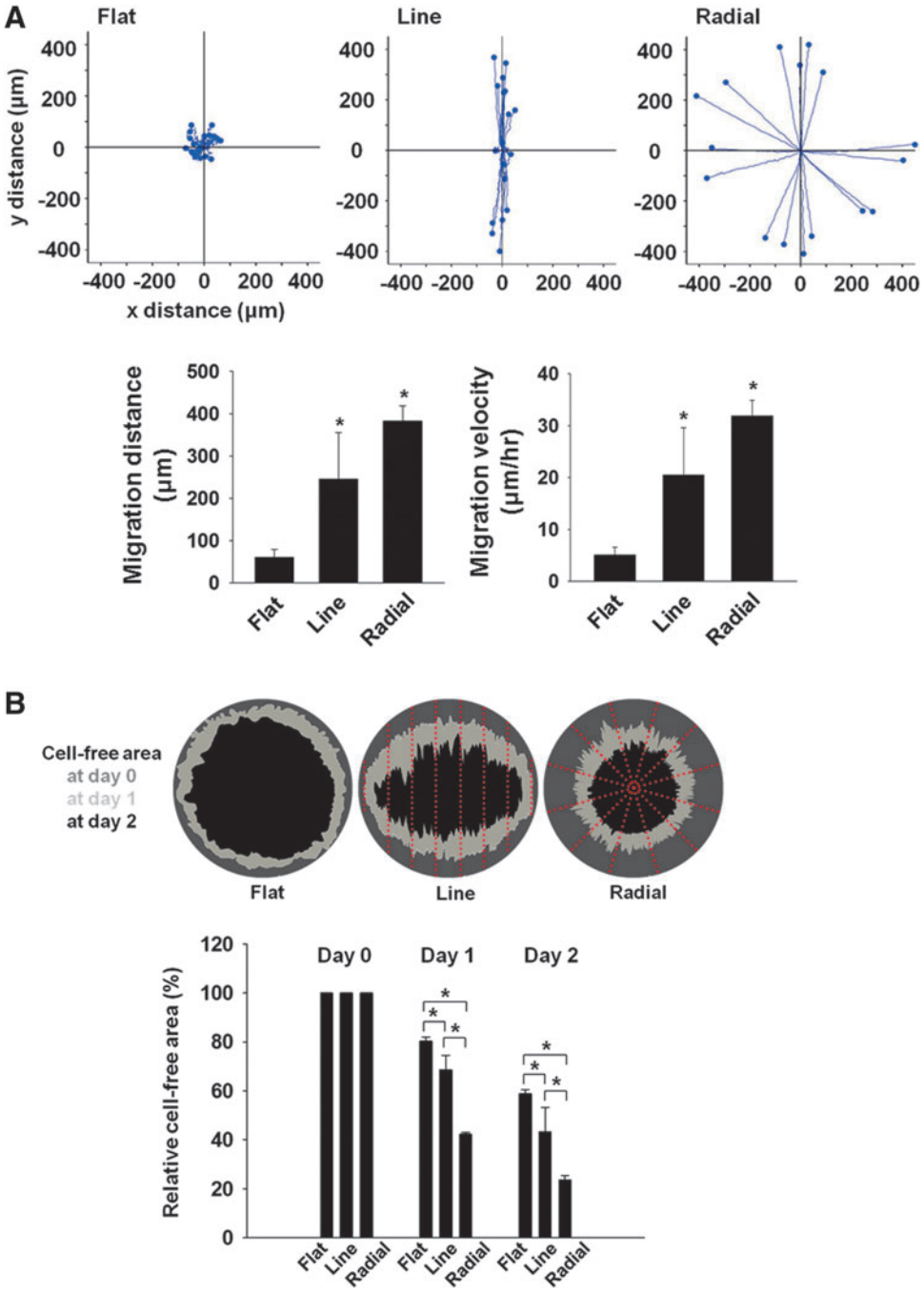

FIG. 5. *In vitro* cell migration on TIs. **(A)** The trajectory, distance, and velocity of MC3T3-E1 cell migration on three different types of TIs as evaluated by time lapse video microscopy. The positions of 16 migrating cells randomly selected on each TI were recorded for 12 h with 15-min intervals. The migration speed of the random cells was quantified by dividing the migration distance by 12 h ($n = 16$ cells per group, $*p < 0.05$ versus flat). **(B)** The cell-free area on the TIs after *in vitro* cell migration for 0, 1, and 2 days ($n = 3$, $*p < 0.05$). Color images available online at www.liebertpub.com/tea

For the *in vitro* cell migration assay on the three different TIs, the cell-free area was determined after cell migration for 1 or 2 days (Fig. 5B). At day 2, 80% of the area was covered by the migrating MC3T3-E1 cells on the radial TI, whereas only 40% and 60% of the area were covered by cells on the flat and line TIs, respectively.

Expressions of intracellular signaling molecules responsible for the cell migration

To investigate the intracellular signaling changes triggered by guided cellular migration, the levels of proteins responsible for the cell migration (E-cadherin, PI3K, pAkt, Akt, and Rac1) were evaluated by western blot analysis (Fig. 6). MC3T3-E1 cells migrating on the line and radial TIs expressed a lower level of E-cadherin and higher levels of PI3K, pAkt/Akt, and Rac1 than did those of the flat TI.

Enhanced proliferation on TIs

In addition to the fast migration of host osteogenic cells to the defect site, fast proliferation into the defect site is an important factor for effective bone repair. The proliferation of MC3T3-E1 cells on the TIs was evaluated by analysis of PCNA protein expression on day 2 (Fig. 7). The western blot analysis showed that the cells on the line and radial TIs proliferated significantly faster than did those on the flat TI.

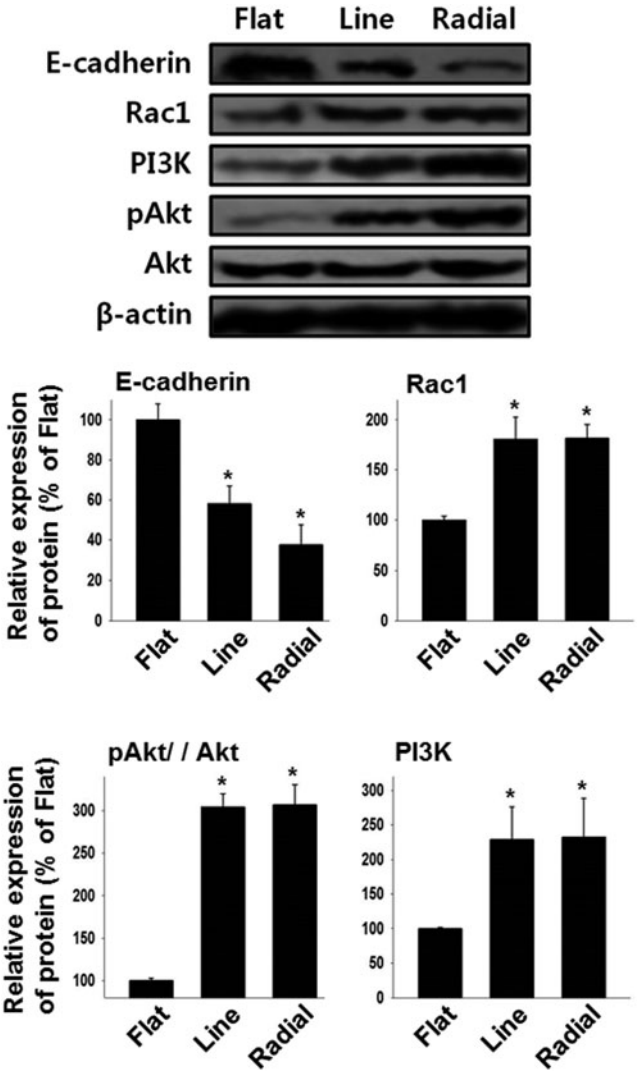

FIG. 6. Enhanced cell migration-related intracellular signaling by microgrooved TIs. The expressions of intracellular signaling molecules responsible for the cell migration were evaluated by western blot analysis ($n=4$, $^*p<0.05$ vs. flat).

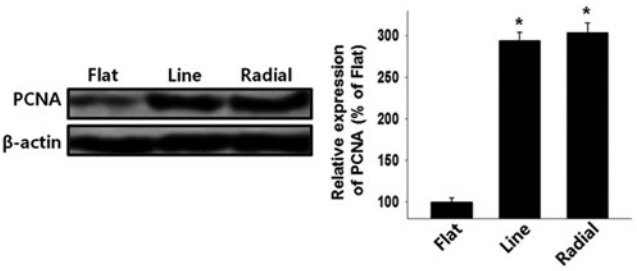

FIG. 7. Enhanced cell proliferation on microgrooved TIs as evaluated by western blot analysis for PCNA expression during cell migration on day 2 ($n=4$, $^*p<0.05$ vs. flat). PCNA, proliferating cell nuclear antigen.

In vivo *bone formation assay*

Based on the *in vitro* cellular behaviors on the TI with radially defined topography, we then investigated whether the radial TI induced more *in vivo* bone repair than did the other types of implants. For this purpose, the three types of TIs were implanted in mouse calvarial defects (Fig. 8A). Seven weeks after implantation, the bone repair was evaluated by micro-CT examination (Fig. 8B) and histological analysis with Goldner's trichrome staining (Fig. 8C). The analyses revealed that the radial TIs showed the best bone repair efficiency, followed by the line TI. In contrast, a very small extent of bone repair was observed with the flat TI.

Discussion

Recruiting host reparative cells to the defect site is a prerequisite step for natural tissue repair.[1–3] For bone reparation in particular, faster recruitment of osteoblasts to the defect site can significantly reduce the time required for bone matrix remodeling and can thus enhance bone reconstruction. Upon bone tissue damage *in vivo*, endogenous osteoblasts are recruited to the lesion site, where chemotactic growth factors, such as TGF-β, BMPs, insulin-like growth factors, vascular endothelial growth factor, and PDGF, are released.[27,28] Based on such findings, a number of previous studies have utilized exogenous growth factors to expedite the recruitment of osteoblasts to the damaged site for a better therapeutic outcome.[5–8] However, growth factors are quite costly, and a high dose is required for *in vivo* applications. In addition, an overdose of growth factors may cause bone overgrowth.[10] To overcome these problems, we proposed a new approach to enhance the osteoblast migration without the use of chemotactic growth factors for bone repair. This study demonstrates that the recruitment of osteoblasts to the damaged lesion can be greatly promoted by the scaffolds with radial microgroove topography. Also, the current study presents the intercellular signaling mechanisms for a better understanding of the migratory behaviors of osteoblasts on microgrooved topographies.

We used NOA 86, a polyurethane-based polymeric material, to fabricate TIs that are compatible with the native

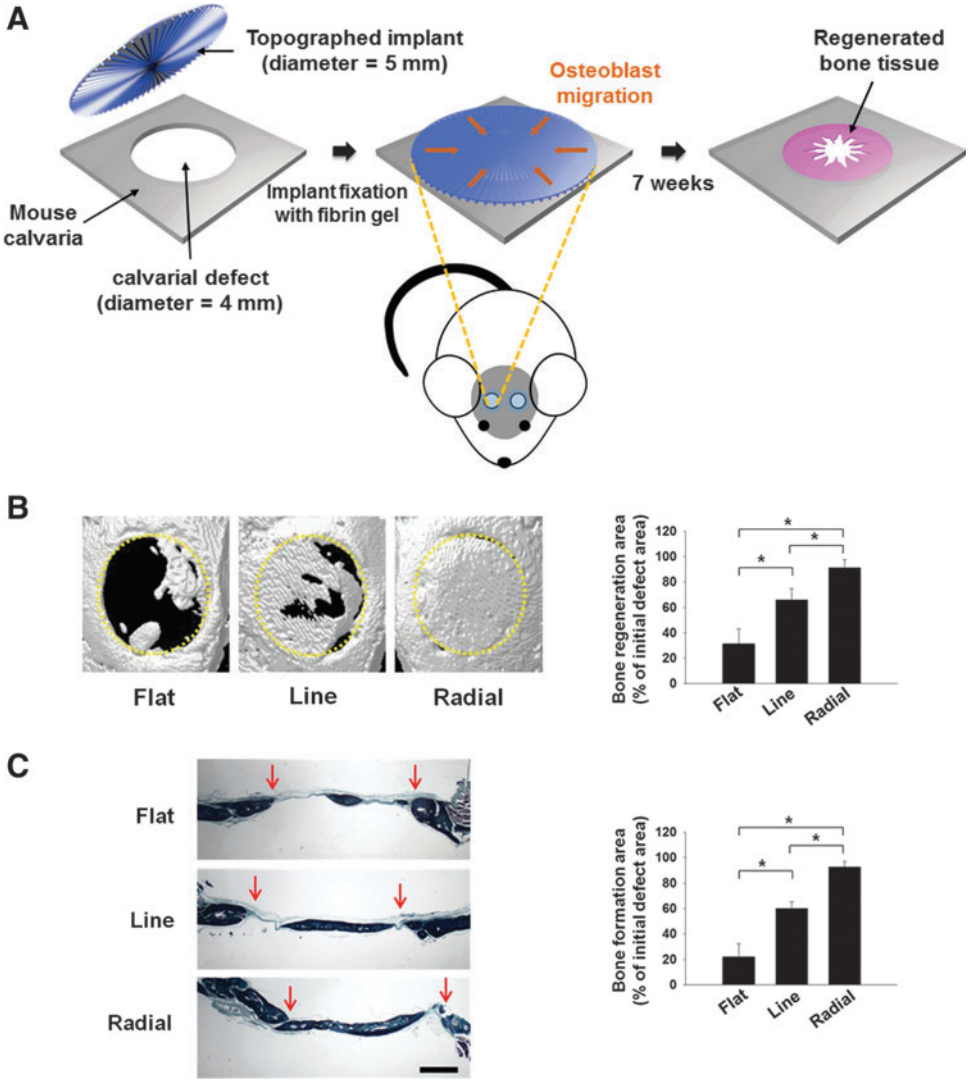

FIG. 8. *In vivo* bone reparation by implanting three different types of TIs for 7 weeks. **(A)** Schematic diagram of implanting TIs in mouse calvarial defects. **(B)** Bone reparation evaluated by micro-CT analysis. Representative micro-CT images of each type of TI implanted in the calvarial defect. *Yellow dotted lines* indicate the original defect margins. The calcified area was determined from the micro-CT images ($n=8$, $*p<0.05$). **(C)** Bone reparation evaluated by histological analysis with Goldner's trichrome staining. *Red arrows* indicate the original defect margins. Scale bar indicates 1 mm. The area of bone reparation was determined by histomorphometric analysis ($n=8$, $*p<0.05$). Color images available online at www.liebertpub.com/tea

bone tissue because the material has proper physiochemical properties for the application of bone tissue engineering. NOA 86 is a rigid polymer with an elastic modulus of approximately 2484 MPa,[29] which is similar to that of natural calvaria (2413 ± 1448 MPa).[30] This is particularly important because previous studies have demonstrated that tissue repair is greatly promoted by scaffolds that have an elastic modulus similar to that of the natural tissue.[31] In addition, cell migration is known to be faster on rigid substrates than on soft substrates with a low elastic modulus.[32,33] Moreover, unlike other rigid polymers, UV-curable NOA 86 can be fabricated easily into multiscale patterns in a reproducible manner and bent to cover the curved surface of the bone defect. To provide the NOA 86-derived TIs with osteoconductivity for better bone repair, the TIs were coated with calcium phosphate. The NOA 86-derived TIs showed no cytotoxicity to osteoblasts (Fig. 3), making it a suitable biomaterial for bone reparative applications.

To assess the recruitment of osteoblasts and evaluate their migratory behaviors on TIs, we mimicked the *in vivo* process of bone repair in calvarial defects with an *in vitro* migration assay (Fig. 4). From the *in vitro* assay, we observed enhanced migratory behaviors of osteoblasts on line or radial TIs compared with the flat TI (Fig. 4A). In addition, cells cultured on line or radial TIs showed a spindle-shaped morphology toward the direction of the microgroove topography (Fig. 4B). These data are in accordance with a previous study, which showed that the directional cell migration is related with the spindle-like structure of the cells.[34] Further evaluation of the osteoblast migratory behavior using time lapse microscopy showed that the cells cultured on line or radial TIs tended to migrate faster toward the direction of the microgroove topography (Fig. 5A). This is particularly intriguing because such phenomenon is similar to the *in vivo* cell migratory behavior where the cells migrate in the direction of the topography of ECM during tissue repair.[34]

We investigated the intracellular signaling mechanisms of the migrating cells on TIs. Previous studies showed that directed cell migration is associated with the Rac1/PI3K/Akt mechanism.[35,36] PI3K and Rac1 proteins are known to be involved in cell polarization, where PI3K acts as a key factor for chemotaxis and Rac1 acts as a downstream effector of PI3K to stimulate the formation of actin filaments

at the leading edge of the migrating cells.[35,36] Other studies have also demonstrated that the motility of the cells is affected by the upregulation of PI3K[37] and Rac1.[38] Furthermore, it has been known that cell migration is affected by the expression of pAkt and Rac1 because the knockdown of these proteins can decrease the motility of the cells.[39,40] In accordance with previous studies, we observed that osteoblasts with directed and accelerated migration on line or radial TIs (Fig. 5A) showed a significant upregulation of Rac1, PI3K, and pAkt (Fig. 6).

In addition to the enhanced migratory behavior of osteoblasts, the line and radial TIs also promoted the cell proliferation. It has been demonstrated that E-cadherin, a cell-to-cell junction protein, is responsible not only for cell migration[41,42] but also for cell proliferation.[41] Previous studies showed E-cadherin directly regulates cell migration and proliferation; thus, the downregulation of E-cadherin enhances cell migration[41,42] and proliferation.[43] In the present study, we observed that osteoblasts on line or radial TIs exhibited a faster migration toward the cell-free area (Fig. 5B) and a much greater expression of PCNA, which is a proliferating cell marker (Fig. 7). Conforming to the findings of previous studies, these observations were accompanied by a significant reduction in E-cadherin expression on line and radial TIs (Fig. 6). Based on these data, we believe that the enhanced cell coverage of the cell-free area on line or radial TIs (Fig. 5B) was attributable not only to the fast migration of the cells but also to the enhanced cell proliferation.

Although the line and radial Tis showed similar migratory and proliferative behavior of the cells, the radial TI showed better performance in the *in vitro* cell coverage assay (Fig. 5B) and the *in vivo* bone repair (Fig. 8). We believe that this finding is due to the difference in the topographical direction between line and radial TIs. Compared with the line TI, the radial TI showed a better, center-focused migration of osteoblasts (Fig. 5B). These data demonstrate that in addition to the microgroove topography that affects the migratory behavior of the cells (Fig. 5A), the directional arrangement of the topography is also a critical factor in cell-free area coverage (Fig. 5B) and bone reconstruction (Fig. 8B).

Conclusion

In this study, we fabricated microgrooved, bone-reparative patches that can efficiently promote the migration and proliferation of osteoblasts and *in vivo* bone repair. We chose NOA 86, which is a rigid, UV-curable, and noncytotoxic material, to fabricate TIs and provided osteoconductivity to the TIs through a calcium phosphate coating. Both line and radial TIs promoted the migration and proliferation of osteoblasts by PI3K/pAkt/Rac1 or the E-cadherin mechanism. However, the radial TI showed better performance in filling the cell-free area *in vitro* and in bone repair *in vivo* compared with the line TI due to the directional arrangement of its topography toward the center of the cell-free area or defect area. Herein, we showed that TIs can promote osteoblast migration and bone repair without the use of growth factors. Our results suggest that TIs with microgrooved topography can be used to promote bone repair by regulating the migratory behaviors of osteogenic cells on TIs.

Acknowledgments

This research was supported by the Korea Health Industry Development Institute (KHIDI), Ministry of Health and Welfare (HI14C3270, HI15C0498, and HI14C1550), Republic of Korea, and National Research Foundation of Korea (015R1A2A1A09005662).

Disclosure Statement

No competing financial interests exist.

References

1. Hernandez-Gil, I.F.T., Gracia, M.A.A., del Canto Pingarrón, M., and Jerez, L.B. Physiological bases of bone regeneration I. Histology and physiology of bone tissue. Med Oral Patol Oral Cir Bucal **11,** E47, 2006.
2. Einhorn, T.A. The cell and molecular biology of fracture healing. Clin Orthop Relat Res **355,** S7, 1998.
3. Schindeler, A., McDonald, M.M., Bokko, P., and Little, D.G. Bone remodeling during fracture repair: the cellular picture. Semin Cell Dev Biol **19,** 459, 2008.
4. Chen, F.M., Wu, L.A., Zhang, M., Zhang, R., and Sun, H.H. Homing of endogenous stem/progenitor cells for in situ tissue regeneration: promises, strategies, and translational perspectives. Biomaterials **32,** 3189, 2011.
5. Hughes, F.J., Aubin, J.E., and Heersche, J.N. Differential chemotactic responses of different populations of fetal rat calvaria cells to platelet-derived growth factor and transforming growth factor beta. Bone Miner **19,** 63, 1992.
6. Lind, M., Deleuran, B., Thestrup-Pedersen, K., Soballe, K., Eriksen, E.F., and Bunger, C. Chemotaxis of human osteoblasts. Effects of osteotropic growth factors. APMIS **103,** 140, 1995.
7. Mehrotra, M., Krane, S.M., Walters, K., and Pilbeam, C. Differential regulation of platelet-derived growth factor stimulated migration and proliferation in osteoblastic cells. J Cell Biochem **93,** 741, 2004.
8. Lind, M., Eriksen, E.F., and Bunger, C. Bone morphogenetic protein-2 but not bone morphogenetic protein-4 and -6 stimulates chemotactic migration of human osteoblasts, human marrow osteoblasts, and U2-OS cells. Bone **18,** 53, 1996.
9. Takata, T., Wang, H.L., and Miyauchi, M. Migration of osteoblastic cells on various guided bone regeneration membranes. Clin Oral Implants Res **12,** 332, 2001.
10. Poynton, A.R., and Lane, J.M. Safety profile for the clinical use of bone morphogenetic proteins in the spine. Spine **27,** S40, 2002.
11. Flemming, R.G., Murphy, C.J., Abrams, G.A., Goodman, S.L., and Nealey, P.F. Effects of synthetic micro- and nano-structured surfaces on cell behavior. Biomaterials **20,** 573, 1999.
12. Bettinger, C.J., Langer, R., and Borenstein, J.T. Engineering substrate topography at the micro- and nanoscale to control cell function. Angew Chem Int Ed Engl **48,** 5406, 2009.
13. Kim, D.H., Seo, C.H., Han, K., Kwon, K.W., Levchenko, A., and Suh, K.Y. Guided cell migration on microtextured substrates with variable local density and anisotropy. Adv Funct Mater **19,** 1579, 2009.
14. Choi, S.J., Yoo, P.J., Baek, S.J., Kim, T.W., and Lee, H.H. An ultraviolet-curable mold for sub-100-nm lithography. J Am Chem Soc **126,** 7744, 2004.
15. Yoo, P.J., Choi, S.J., Kim, J.H., Suh, D., Baek, S.J., Kim, T.W., and Lee, H.H. Unconventional patterning with a modulus-tunable mold: from imprinting to microcontact printing. Chem Mater **16,** 5000, 2004.

16. Vitale, A., Hennessy, M.G., Matar, O.K. and Cabral, J.T. Interfacial profile and propagation of frontal photopolymerization waves. Macromolecules **48,** 198, 2014.
17. Choi, S.J., Kim, H.N. Bae, W.G., and Suh, K.Y. Modulus- and surface energy-tunable ultraviolet-curable polyurethane acrylate: properties and applications. J Mater Chem **21,** 14325, 2011.
18. Kim, H.N., Kang, D.H., Kim, M.S., Jiao, A., Kim, D.H., and Suh, K.Y. Patterning methods for polymers in cell and tissue engineering. Ann Biomed Eng **40,** 1339, 2012.
19. Abe, Y., Kokubo, T., and Yamamuro, T. Apatite coating on ceramics, metals and polymers utilizing a biological process. J Mater Sci Mater Med **1**, 233, 1990.
20. Kokubo, T., and Takadama, H. How useful is SBF in predicting *in vivo* bone bioactivity? Biomaterials **27,** 2907, 2006.
21. Webster, T.J., Ergun, C., Doremus, R.H., Siegel, R.W., and Bizios, R. Enhanced functions of osteoblasts on nanophase ceramics. Biomaterials **21,** 1803, 2000.
22. Lee, J.M., Kim, E.A., and Im, G.I. Healing of tibial and calvarial bone defect using Runx-2-transfected adipose stem cells. Tissue Eng Regener Med **12,** 107, 2015.
23. Lee, J.H., Kim, C.S., Choi, K.H., Jung, U.W., Yun, J.H., Choi, S.H., and Cho, K.S. The induction of bone formation in rat calvarial defects and subcutaneous tissues by recombinant human BMP-2, produced in Escherichia coli. Biomaterials **31,** 3512, 2010.
24. Suchanek, W., and Yoshimura, M. Processing and properties of hydroxyapatite-based biomaterials for use as hard tissue replacement implants. J Mater Res **13,** 94, 1998.
25. Wang, M. Surface modification of biomaterials and tissue engineering scaffolds for enhanced osteoconductivity. 3rd Kuala Lumpur International Conference on Biomedical Engineering 2006 **15,** 22, 2007.
26. Perez, R.A., Shin, S.H., Han, C.H., and Kim, H.W. Bioactive injectables based on calcium phosphates for hard tissues: a recent update. Tissue Eng Regener Med **12,** 143, 2015.
27. Sims, N.A., and Gooi, J.H. Bone remodeling: multiple cellular interactions required for coupling of bone formation and resorption. Semin Cell Dev Biol **19,** 444, 2008.
28. Tang, Y., Wu, X., Lei, W., Pang, L., Wan, C., Shi, Z., Zhao, L., Nagy, T.R., Peng, X., Hu, J., Feng, X., Van Hul, W., Wan, M., and Cao, X. TGF-beta1-induced migration of bone mesenchymal stem cells couples bone resorption with formation. Nat Med **15,** 757, 2009.
29. Jeon, H., Tsui, J.H., Jang, S.I., Lee, J.H., Park, S., Mun, K., Boo, Y.C., and Kim, D.H. Combined effects of substrate topography and stiffness on endothelial cytokine and chemokine secretion. ACS Appl Mater Interfaces **7,** 4525, 2015.
30. Boruah, S., Henderson, K., Subit, D., Salzar, R.S., Shender, B.S., and Paskoff, G. Response of human skull bone to dynamic compressive loading. Proceedings of the IRCOBI Conference **13,** 497, 2013.
31. Krishna, B.V., Bose, S., and Bandyopadhyay, A. Low stiffness porous Ti structures for load-bearing implants. Acta Biomater **3,** 997, 2007.
32. Lo, C.M., Wang, H.B., Dembo, M., and Wang, Y. Cell movement is guided by the rigidity of the substrate. Biophys J **79,** 144, 2000.
33. Ng, M.R., Besser, A., Danuser, G., and Brugge, J.S. Substrate stiffness regulates cadherin-dependent collective migration through myosin-II contractility. J Cell Biol **199,** 545, 2012.
34. Petrie, R.J., Doyle, A.D., and Yamada, K.M. Random versus directionally persistent cell migration. Nat Rev Mol Cell Biol **10,** 538, 2009.
35. Ridley, A.J., Schwartz, M.A., Burridge, K., Firtel, R.A., Ginsberg, M.H., Borisy, G., Parsons, J.T., and Horwitzl, A.R. Cell migration: integrating signals from front to back. Science **302,** 1704, 2003.
36. Pankov, R., Endo, Y., Even-Ram, S., Araki, M., Clark, K., Cukierman, E., Matsumoto, K., and Yamada, K.M. A Rac switch regulates random versus directionally persistent cell migration. J Cell Biol **170,** 793, 2005.
37. Bosgraaf, L., Keizer-Gunnink, I., and Van Haastert, P.J. PI3-kinase signaling contributes to orientation in shallow gradients and enhances speed in steep chemoattractant gradients. J Cell Sci **121,** 3589, 2008.
38. Monypenny, J., Zicha, D., Higashida, C., Oceguera-Yanez, F., Narumiya, S., and Watanabe, N. Cdc42 and Rac family GTPases regulate mode and speed but not direction of primary fibroblast migration during platelet-derived growth factor-dependent chemotaxis. Mol Cell Biol **29,** 2730, 2009.
39. Higuchi, M., Masuyama, N., Fukui, Y., Suzuki, A., and Gotoh, Y. Akt mediates Rac/Cdc42-regulated cell motility in growth factor-stimulated cells and in invasive PTEN knockout cells. Curr Biol **11,** 1958, 2001.
40. Keely, P.J., Westwick, J.K., Whitehead, I.P., Der, C.J., and Parise, L.V. Cdc42 and Rac1 induce integrin-mediated cell motility and invasiveness through PI(3)K. Nature **390,** 632, 1997.
41. Chen, H., Paradies, N.E., Fedor-Chaiken, M., and Brackenbury, R. E-cadherin mediates adhesion and suppresses cell motility via distinct mechanisms. J Cell Sci, **110,** 345, 1997.
42. Fransvea, E., Angelotti, U., Antonaci, S., and Giannelli, G. Blocking transforming growth factor-beta up-regulates E-cadherin and reduces migration and invasion of hepatocellular carcinoma cells. Hepatology **47,** 1557, 2008.
43. Kim, N.G., Koh, E., Chen, X., and Gumbiner, B.M. E-cadherin mediates contact inhibition of proliferation through Hippo signaling-pathway components. Proc Natl Acad Sci U S A **108,** 11930, 2011.

Address correspondence to:
Byung-Soo Kim, PhD
School of Chemical and Biological Engineering
Seoul National University
Seoul 151-744
Republic of Korea

E-mail: byungskim@snu.ac.kr

Noo Li Jeon, PhD
School of Mechanical and Aerospace Engineering
Seoul National University
Seoul 151-744
Republic of Korea

E-mail: njeon@snu.ac.kr

Received: September 4, 2015
Accepted: March 14, 2016
Online Publication Date: March 30, 2016